

Article

Open Access



High-entropy nitrides from dual entropic and enthalpic forces for high-efficiency oxygen evolution reaction

Jingyun Jiang¹, Yifan Xu², Zheng Wang¹, Hongbo Zhang¹, Qun Xu^{1,3,*}, Yuanjian Li^{4,*}

¹College of Materials Science and Engineering, Zhengzhou University, Zhengzhou 450052, Henan, China.

²School of Materials Science and Engineering, Nanyang Technological University, Singapore 639798, Singapore.

³Henan Institute of Advanced Technology, Zhengzhou University, Zhengzhou 450052, Henan, China.

⁴Institute of Materials Research and Engineering (IMRE), Agency for Science, Technology and Research (A*STAR), Singapore 138634, Singapore.

***Correspondence to:** Prof. Qun Xu, College of Materials Science and Engineering, Zhengzhou University, No. 100 Science Avenue, Zhengzhou 450052, Henan, China; Henan Institute of Advanced Technology, Zhengzhou University, No. 100 Science Avenue, Zhengzhou 450052, Henan, China. E-mail: qunxu@zzu.edu.cn; Dr. Yuanjian Li, Institute of Materials Research and Engineering (IMRE), Agency for Science, Technology and Research (A*STAR), 2 Fusionopolis Way, Singapore 138634, Singapore. E-mail: li_yuanjian@imre.a-star.edu.sg

How to cite this article: Jiang, J.; Xu, Y.; Wang, Z.; Zhang, H.; Xu, Q.; Li, Y. High-entropy nitrides from dual entropic and enthalpic forces for high-efficiency oxygen evolution reaction. *Energy Mater.* 2025, 5, 500019. <https://dx.doi.org/10.20517/energymater.2024.130>

Received: 21 Aug 2024 **First Decision:** 13 Sep 2024 **Revised:** 27 Sep 2024 **Accepted:** 11 Oct 2024 **Published:** 10 Jan 2025

Academic Editor: Soo Young Kim **Copy Editor:** Fangling Lan **Production Editor:** Fangling Lan

Abstract

The development of high-entropy materials as active and durable catalysts for oxygen evolution reaction is important but challenging for hydrogen production from water electrolysis. In contrast to conventional synthesis strategies that usually involve high-temperature annealing, a novel poly(ethylene glycol)-barbituric acid deep eutectic solvent-assisted strategy was developed in this work to successfully synthesize high-entropy nitrides (HENs) (FeCoNiCuZn)N at a record low temperature of 473 K. Multiple analytical characterizations illustrate that dual entropic and enthalpic forces provided by the poly(ethylene glycol)-barbituric acid deep eutectic solvent play a critical role in the low-temperature synthesis of HENs. The prepared HENs have a microsphere structure consisting of five highly dispersed active metal (Fe, Co, Ni, Cu, and Zn) species, which are conducive to boosting oxygen evolution reaction performance in alkaline media, in terms of a low overpotential of 223 mV at 10 mA cm⁻² and sustained durability over 30 h at 400 mA cm⁻². This work paves the way for the fabrication of high-entropy materials with excellent electrocatalytic properties for future energy conversion and storage applications.

Keywords: High-entropy, multi-metal nitride, deep eutectic solvent, low-temperature, oxygen evolution reaction



© The Author(s) 2025. **Open Access** This article is licensed under a Creative Commons Attribution 4.0 International License (<https://creativecommons.org/licenses/by/4.0/>), which permits unrestricted use, sharing, adaptation, distribution and reproduction in any medium or format, for any purpose, even commercially, as long as you give appropriate credit to the original author(s) and the source, provide a link to the Creative Commons license, and indicate if changes were made.



INTRODUCTION

High-entropy materials (HEMs), consisting of five or more metal elements in equal or nearly equal amounts, are attracting significant attention for their unexpected physical and chemical properties, including high entropy effect, lattice distortion effect, and synergistic effect^[1-5]. The HEMs have been widely used in the fields of catalysis, thermoelectric, soft magnetic, and radiation tolerant materials, *etc.*^[6,7]. Notably, the unique intermetallic interaction involved in HEMs provides an expansive and underexplored compositional space for electrochemical applications including batteries, supercapacitors, and electrochemical catalysis^[8-10]. Recent advances have reported that non-noble HEMs, such as (CrMnFeCoNi)S^[11], CrMnFeCoNi^[12], (CoFeNiCrMn)P^[13], NiFeCoMnOOH^[14], (CrFeCoNiMo)₃O₄^[15], and La(CrMnFeCo₂Ni)O₃^[16], show superior catalytic activities than the related non-high-entropy counterparts. More importantly, the catalytic activity of reported HEMs even surpasses that of the noble oxygen evolution reaction (OER) electrocatalysts such as IrO₂ and RuO₂. Therefore, the strategic design of highly efficient HEMs holds great promise for water oxidation and hydrogen production^[17].

Among various HEMs, high-entropy nitrides (HENs) are particularly notable for their exceptional chemical stability and electrical conductivity, making them ideal catalysts for efficient OER performance^[18,19]. Conventional synthesis methods, such as carbothermal shock, electrochemical shock, and forced metal exchange, typically demand complex setups and reaction conditions, often requiring elevated temperatures (typically ranging from 600 to 1,000 K) or pressures^[20-22]. The absence of straightforward and universal methods for fabricating HENs at low temperatures significantly hinders their broader application. In this context, deep eutectic solvents (DESs), formed by the simple mixture of a hydrogen bond donor and a hydrogen bond acceptor in a specific molar ratio, exhibit intriguing features such as highly tailorable compositions, strong solvation abilities, and extended hydrogen-bonding networks^[23]. Consequently, deep eutectic-solvothermal synthesis has emerged as a rapid and cost-effective technique for the controllable synthesis of various functional multi-metal-based materials^[24-26]. However, there were few works that focused on the synthesis mechanism, especially on the relationship between the design of DESs and the functionality of achieved multi-metal-based materials.

In this work, a novel HEN (FeCoNiCuZn)N with a single phase was synthesized in the designed polyethylene glycol-barbituric acid DES (PBDES) at a low temperature of 473 K. Further, the thermal characterizations illustrate the feasibility of the successful formation of (FeCoNiCuZn)N. The prepared (FeCoNiCuZn)N has a microsphere structure that consists of five highly dispersed metal species. Among them, Co has a higher oxidation state with the incorporation of Fe, Ni, Cu, and Zn, which are positive for the improvement of OER activity. Meanwhile, the multiple active components in the obtained (FeCoNiCuZn)N, equipped with a high-entropy stabilization effect, exhibit outstanding OER durability (without activity decay over 30 h at 400 mA cm⁻²). The extraordinary activity and stability demonstrate the great potential of (FeCoNiCuZn)N as a practical OER electrocatalyst for water splitting. The innovation of our low-temperature method highlights its potential advantages, particularly in terms of energy savings and scalability for practical applications.

EXPERIMENTAL

Materials

Polyethylene glycol (PEG) 200, Co(NO₃)₂·6H₂O (≥ 99%), barbituric acid (BA), potassium hydroxide (KOH, ≥ 90%), and ethanol were sourced from Sinopharm Chemical Reagent Co., Ltd. Fe(NO₃)₂·9H₂O (99.99%), Zn(NO₃)₂·6H₂O (99.99%), and Ni(NO₃)₂·6H₂O (99.99%) were acquired from Shanghai Aladdin Biochemical Technology Co., Ltd., while Cu(NO₃)₂·3H₂O (99%) and ruthenium oxide (RuO₂, 99.9%) were obtained from Shanghai Macklin Biochemical Co., Ltd. All chemicals were used without further purification, and ultrapure

water with a resistivity of 18.2 M Ω -cm was used in all experiments.

Preparation of (FeCoNiCuZn)N and the related single metal nitrides

(FeCoNiCuZn)N was obtained via a one-step eutectic-solvothermal process. Typically, 2 mmol each of Fe(NO₃)₃·6H₂O, Co(NO₃)₂·6H₂O, Ni(NO₃)₂·6H₂O, Cu(NO₃)₂·6H₂O, and Zn(NO₃)₂·6H₂O were dissolved in 30 mL PBDESS. The formed dark-brown solution was then transferred into a 100 mL Teflon-lined autoclave and heated at 200 °C for 16 h. After cooling, the samples were collected, washed and dried at 60 °C for 2 h. In addition, unary metal nitrides (UMNs) were synthesized using the same method as for (FeCoNiCuZn)N, dissolving 10 mmol of each corresponding nitrate in PBDESS.

Materials characterization

Thermal analysis was conducted using a METTLER TOLEDO TGADSC3+ (Germany) system, with a heating rate of 3 °C min⁻¹ from 30 to 450 °C under an Argon atmosphere. Fourier transform infrared spectroscopy (FT-IR) was performed on a Shimadzu Prestige 21 (Japan, DTGS detector) using the KBr pellet technique, with a measurement range of 750 to 4,000 cm⁻¹. Raman spectra were obtained using a LabRAM HR Evolution with a 638 nm laser.

Scanning electron microscopy (SEM) was carried out using a Hitachi SU8010 field emission SEM (Japan), while transmission electron microscopy (TEM) and high-resolution TEM (HRTEM) were performed using an FEI Tecnai G2 F20 field emission microscope. Dark-field scanning TEM (STEM) was performed on FEI Themis Z, Titan Cubed Themis G2300, JEM-ARM200F.

X-ray powder diffraction (XRD) was done with a Y-2000 diffractometer ($\lambda = 1.5406 \text{ \AA}$) using Cu K α radiation at a scanning rate of 5° min⁻¹. X-ray photoelectron spectroscopy (XPS) was conducted using a Thermo Fisher Scientific ESCA Lab250 (USA) with an Al K α source. All XPS data were calibrated using the C 1s line at 284.6 eV and fitted using the Gaussian fitting method.

X-ray absorption near-edge structure (XANES) and X-ray absorption fine structure (XAFS) spectra were collected at the TPS44A1 beamline of the National Synchrotron Radiation Research Center (NSRRC), operating at 3.5 GeV with a constant current of 260 mA. The energy calibration was performed using Co foil. Data extraction and line fitting were conducted using the Athena and Artemis software. For XANES, the absorption coefficients $\mu(E)$ were processed through background subtraction and normalization, reported as “normalized absorption” with E_0 for all samples. XAFS Fourier-transformed (FT) data in R space were analyzed using the Co foil model for Co-Co contributions. The passive electron factors (S_0) were determined by fitting the Co foil data with a fixed Co-Co coordination number (CN) and then applied to the analysis of the measured samples.

Electrochemical performances

All electrochemical experiments were performed using a CHI 760E electrochemical station (ChenHua Instrument, Shanghai, China) in a three-electrode configuration. The OER performance was evaluated in 1 M KOH, with (FeCoNiCuZn)N-modified glassy carbon and Ni foam as the working electrodes, a graphite rod as the counter electrode, and an Ag/AgCl electrode (in saturated KCl) as the reference. For comparison, UMN-modified glassy carbon electrodes were also tested. All potentials were calibrated against the reversible hydrogen electrode (RHE) using $E_{(RHE)} = E_{(Ag/AgCl)} + 0.197 \text{ V} + 0.059 \times \text{pH}$, and polarization curves were corrected for 80% iR drop.

Linear sweep voltammetry (LSV) was performed from 1.0 to 1.7 V vs. RHE at a scan rate of 5 mV s⁻¹. Tafel slopes were derived from the LSV curves. Cyclic voltammetry (CV) was conducted at scan rates ranging from 1 to 200 mV s⁻¹ within a potential window of -0.1 to 0.1 V (vs. Ag/AgCl), where only non-faradaic currents were observed. Electrochemical impedance spectroscopy (EIS) was measured in potentiostatic mode over a frequency range of 0.1 to 100 kHz. Electrochemical stability tests of the samples were performed by utilizing multi-potential steps, multi-current steps and amperometry i-t experiments.

RESULTS AND DISCUSSION

Fabrication of HENs (FeCoNiCuZn)N

DES-aided strategy for HEN synthesis at low-temperature can be schematically generalized with an associated Gibbs free energy (ΔG) [Figure 1A]. The decomposing ΔG° involves an enthalpy contribution (ΔH) and an entropy contribution ($T\Delta S$), and it must be negative under the experimental conditions. In detail, the differential scanning calorimetry (DSC) curves [Figure 1B] of PBDESs with or without metal salts reveal their related endothermic peaks. For PBDESs, an endothermic peak at 473 K is observed, indicating PBDESs intensively decomposed at 473 K, which is in accordance with the thermogravimetric analysis (TGA) results [Supplementary Figure 1]. For comparison, the thermal destruction of salt-in-PBDESs becomes less intensive, as proved by the decreased decomposition enthalpy and reduced decomposed temperature. The normalized decomposition enthalpies of PBDESs with or without five metal salts are -332.99 and -201.06 J g⁻¹, respectively. In other words, in the presence of metal salts, the endo effect of thermo-destruction occurs at lower temperatures and the enthalpy value decreases by 1.5-fold. In addition, the minimum endothermic peak for the decomposition shifts from 473 to 458 K [Figure 1B, Supplementary Figure 1]. The lower temperature and enthalpy peak of the pyrolysis process indicate that the salts-in-PBDES system has a less perfectly ordered structure, which is caused by the interaction between metal ions and PBDESs. Apart from the enthalpy contribution, a substantial positive entropy change arises from the increased degree of disorder. Under ideal mixing conditions, the entropy could be calculated by $\Delta S_{mix} = -R \sum_{i=1}^n X_i \ln X_i$, where X_i represents the molar fraction of each element in the system and R is the gas constant. The configurational entropy of five salts-in-PBDES and PBDES is -13.381 and 0 J K⁻¹ mol⁻¹, respectively [Figure 1C]. During the pyrolysis of PBDES in the presence of metal salts, the reaction proceeds through multiple thermal stages, including distinct endothermic and exothermic events. These thermal transitions play a crucial role in forming HENs at a record low temperature of 473 K. The decomposition of PBDES, coupled with the controlled release of gases, enhances reaction kinetics, facilitating the formation of the nitrides at this low temperature. The efficient assembly interaction between metal salts and PBDESs was realized in the homogeneous salts-in-PBDES system, which can be proved by the Fourier transform-infrared spectroscopy (FT-IR) [Supplementary Figure 2, Figure 1D] and Raman results [Figure 1E]. As depicted in Supplementary Figure 2, the -OH peak derived from PEG 200 shifts from 3,406 to 3,386 cm⁻¹, and the related half peak width is increased, suggesting the formation of a supramolecular network via H bonding between the -OH group and the C=O group. After adding metal salts, the asymmetric stretching peak of -C=O in Figure 1D shifts from 1,720 cm⁻¹ to approximately 1,738 cm⁻¹, which is caused by the complexation between metal ions and BA^[27]. Additionally, the complexation is further proved by Raman result. As Figure 1E depicts, a new band at 1,038 cm⁻¹ is attributed to the M-N complex^[28,29]. The complex interaction between metal ions and BA as well as the BA-PEG hydrogen bonding interaction are thermally in favor of the pyrolysis process. Furthermore, the generation of high-temperature conditions is caused by the combustion of volatile and light species accompanied by the cracking, dehydrogenation, and dealkylation of PBDES, providing sufficient thermal energy^[30,31] for multielement metal nitride formation. Therefore, the synthesis of PBDES-assisted HMNs begins with the pyrolysis of PBDES in the presence of metal salts. This process involves a series of endothermic and exothermic steps, ultimately resulting in the formation of the target (FeCoNiCuZn)N at a relatively low temperature of 473 K.

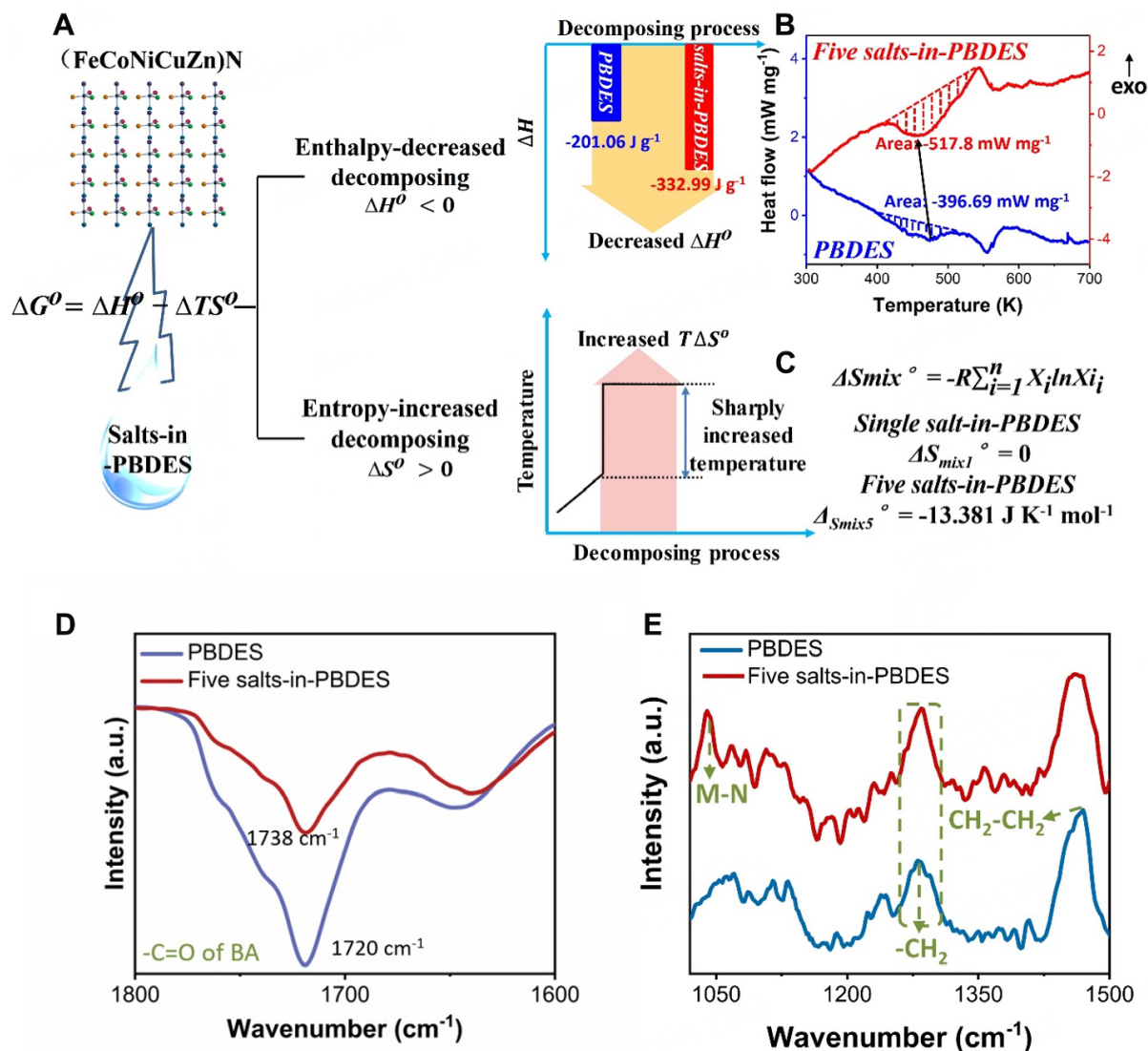


Figure 1. Schematic representation of the formation of (FeCoNiCuZn)N via a low-temperature solvothermal process. (A) Schematic mechanism of (FeCoNiCuZn)N; (B) DSC results and (C) the calculated entropy values, (D) Magnified FT-IR spectrum, and (E) Raman spectrum of salts-in-PBDES and PBDES systems. PBDES: Polyethylene glycol-barbituric acid deep eutectic solvent.

Structural and compositional characterization

To elucidate the crystallographic properties of the prepared HENs, powder X-ray diffraction (PXRD) analysis was conducted [Figure 2A]. The obtained data closely match the hexagonal FeN_{0.0589} phase (JCPDS 01-075-2130), with a space group of P63/mmc (No. 194), confirming the successful formation of single-phase nitrides. Despite the low concentration of nitrogen atoms integrated into the metal lattice in this structure, the material is designated as (FeCoNiCuZn)N to emphasize its composition and highlight its high-entropy characteristics. To further investigate the structure of (FeCoNiCuZn)N, SEM and TEM technologies were utilized. Figure 2B and C shows that the average size of the HEN nanoparticle is approximately 100 nm. This uniform size is primarily due to the templating effect of PEG 200, a common surfactant, which not only regulates nanoparticle size but also reduces agglomeration and enhances the stability of the synthesized nanoparticles. HRTEM images [Figure 2D] depict clear lattice fringes, indicative of the high crystallinity of (FeCoNiCuZn)N. The observed interplanar spacing of 0.21 nm [Inset of Figure 2D] corresponds well with the d(111) plane of FeN_{0.0589}, which exhibits a hexagonal crystal structure

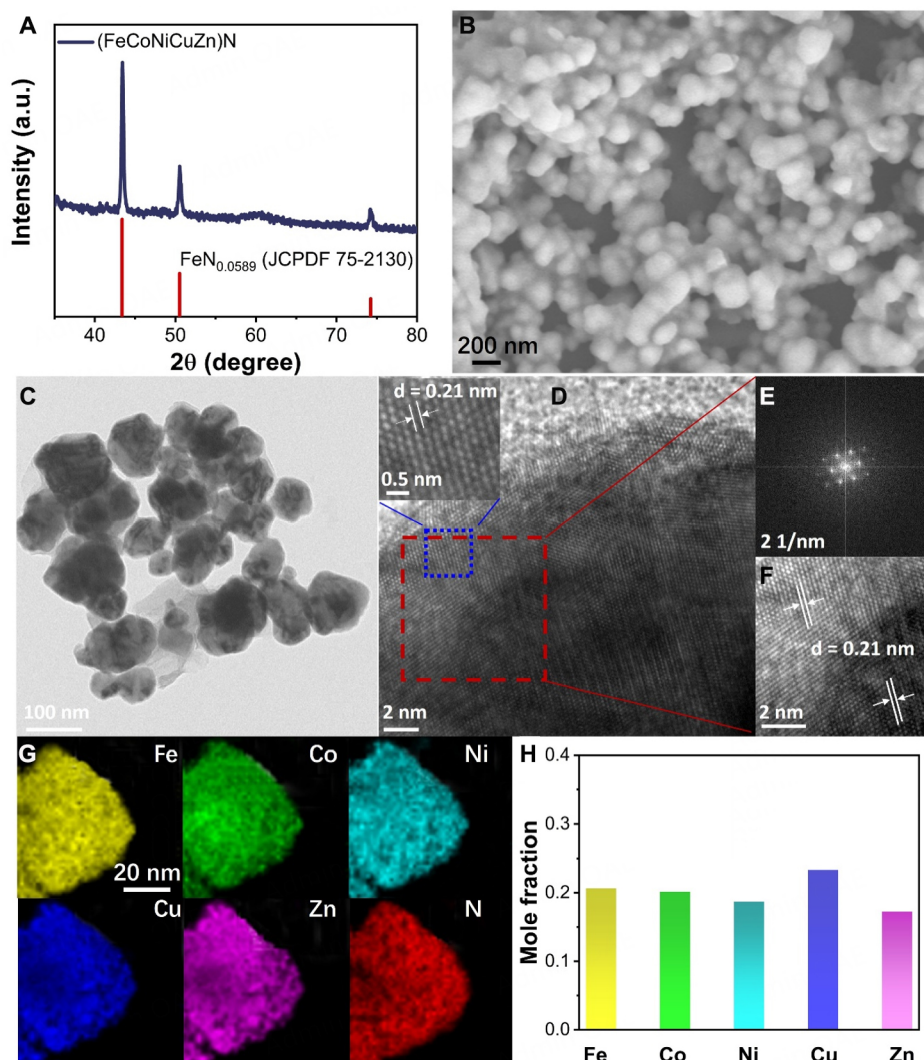


Figure 2. Structural characterization of (FeCoNiCuZn)N. (A) PXR D pattern, (B) SEM, (C) TEM and (D) HRTEM images of (FeCoNiCuZn)N; Inset (D) was the magnified area in blue region. (E) FFT and (F) IFFT pattern of the red region derived from (D); (G) EDS elemental mapping of (FeCoNiCuZn)N: Fe (yellow), Co (green), Ni (cyan), Cu (blue), Zn (purple) and N (red); (H) Mole fraction of (FeCoNiCuZn)N obtained from the ICP-AES result.

and is well consistent with the XRD results. This is further corroborated by the fast Fourier transformation (FFT) image [Figure 2E] and inverse FFT (IFFT) pattern [Figure 2F]. Additionally, the uniform distribution of the five metal species (Fe, Co, Ni, Cu, and Zn) and the non-metal element (N) was visualized by energy-dispersive X-ray (EDX) mapping [Figure 2G] and inductively coupled plasma atomic emission spectrometry (ICP-AES) results [Figure 2H, Supplementary Table 1].

The elemental composition and chemical states of (FeCoNiCuZn)N were analyzed using XPS. The full survey spectrum [Supplementary Figure 3] proves the presence of Fe, Co, Ni, Cu, Zn, N, C, and O in the synthesized material. The high-resolution Fe 2p spectrum [Figure 3A] reveals two spin-orbit doublets and four shake-up satellites^[32]. The first doublet at 712.4 and 725.5 eV corresponds to Fe³⁺, while the second at 710.3 and 723.4 eV is attributed to Fe²⁺. In the high-resolution Co 2p spectrum [Figure 3B], four subpeaks corresponding to Co²⁺ and Co³⁺ are deconvoluted, with peaks at 780.2 and 795.6 eV for Co³⁺, and 781.3 and 798.0 eV for Co²⁺^[27]. Similarly, the co-existence of Ni²⁺ and Ni³⁺ in (FeCoNiCuZn)N is also confirmed by the

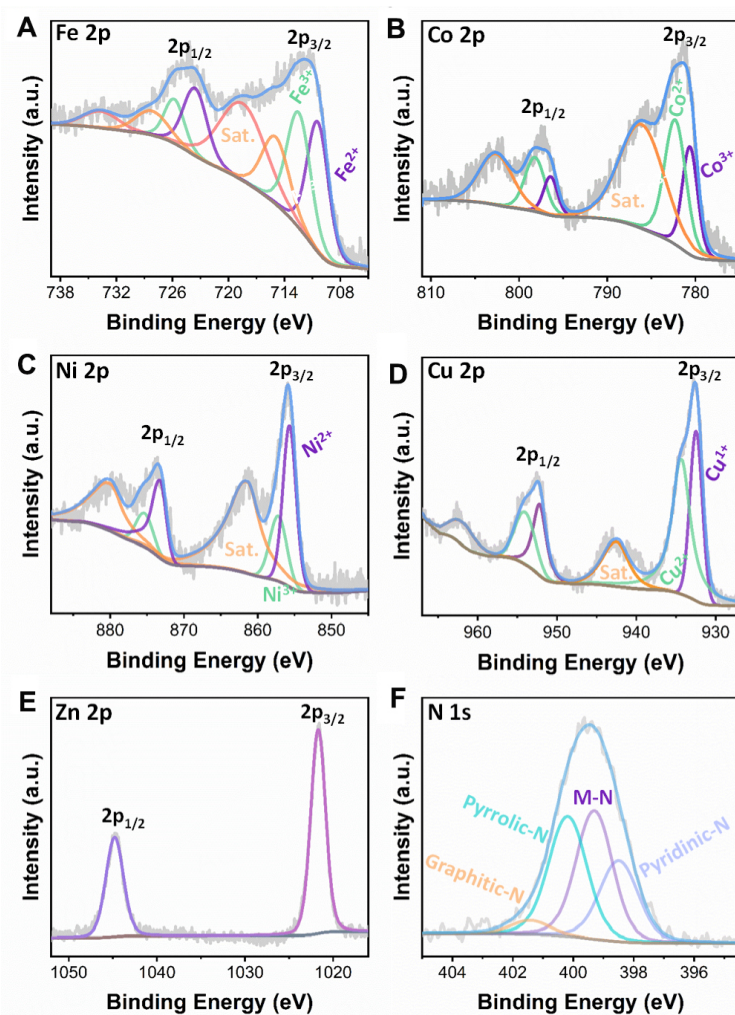


Figure 3. XPS spectra of (FeCoNiCuZn)N: (A) Fe 2p, (B) Co 2p, (C) Ni 2p, (D) Cu 2p, (E) Zn 2p, and (F) N 1s.

high-resolution Ni 2p spectrum [Figure 3C], where the peaks located at 854.6 and 872.0 eV are related to Ni²⁺, and those at 856.4 and 873.9 eV corresponded to Ni³⁺[33]. The Cu 2p spectrum [Figure 3D] shows Cu 2p_{3/2} (934.2 eV), Cu 2p_{1/2} (953.9 eV), and a characteristic shake-up peak (942–944 eV) indicative of Cu²⁺[34]. The Zn 2p spectrum [Figure 3E] displays two spin-orbit peaks at 1,045.7 and 1,022.5 eV, corresponding to Zn²⁺ 2p_{3/2} and 2p_{1/2}, respectively[35]. In the N 1s spectrum [Figure 3F], four distinct peaks appear at binding energies of 398.5, 399.3, 400.2 and 401.4 eV. These peaks correspond to pyridinic nitrogen, nitrogen-metal bonds, pyrrolic nitrogen, and graphitic nitrogen, respectively[36]. The valence states of nitrogen in pyridinic, nitrogen-metal, and pyrrolic forms are -3, while graphitic nitrogen exhibits a valence state of 0 due to differences in bonding environments, ensuring the overall charge balance within the systems.

Evaluation of electrocatalytic performance

To identify the structural advantages of the obtained samples, the electrochemical behaviors of (FeCoNiCuZn)N and related UMNs including (Fe)N, (Co)N, (Ni)N, (Cu)N, and (Zn)N were compared and evaluated utilizing a classical three-electrode system in 1 M KOH. LSV curves of all samples were listed in Figure 4A and Supplementary Figure 4. The OER activity of (FeCoNiCuZn)N outperforms all the related UMNs, performing an excellent overpotential of 223 mV (at 10 mA cm⁻²) and 328 mV (at 100 mA cm⁻²).

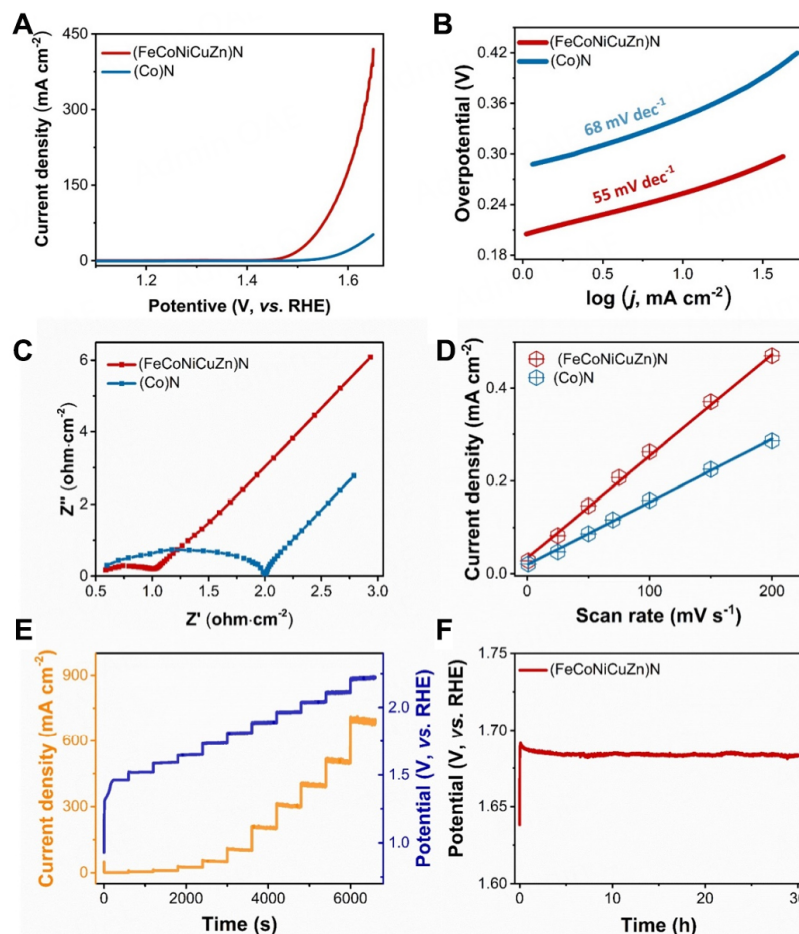


Figure 4. Electrochemical performance of the obtained samples. (A) Geometrical area normalized LSV curves, (B) Tafel plots, (C) EIS, and (D) EASA results of (FeCoNiCuZn)N (red) and (Co)N (blue) modified glass carbon electrodes; (E) Multi-potential steps (left, orange) and multi-current steps (right, blue) of (FeCoNiCuZn)N; (F) Chronopotentiometry curve of (FeCoNiCuZn)N modified Ni foam at current density located at 400 mA cm^{-2} for 30 h.

This performance is also superior to those of previously reported transition metal-based materials [Supplementary Table 2]. Furthermore, the kinetic processes of those catalysts were also evaluated by the Tafel slopes derived from the LSV curves [Figure 4B]. The Tafel slopes of those samples follow this order: (FeCoNiCuZn)N (57 mV dec^{-1}) < (Co)N (68 mV dec^{-1}) < (Ni)N (71 mV dec^{-1}) < (Fe)N (90 mV dec^{-1}) < (Cu)N (91 mV dec^{-1}) < (Zn)N (92 mV dec^{-1}). To investigate the OER kinetics, EIS tests of (FeCoNiCuZn)N and (Co)N were performed and the Nyquist plots were shown in Figure 4C. Apparently, (FeCoNiCuZn)N exhibits a relatively low charge transfer resistance (R_{ct}) value, which is much lower than that of (Co)N. Moreover, the electrochemically active surface area (ECSA) was calculated [Figure 4D and Supplementary Figure 5]. The double-layer capacitances (C_{dl}) of (FeCoNiCuZn)N and (Co)N are determined to be 0.0022 and $0.0013 \text{ mF cm}^{-2}$, respectively, indicating that (FeCoNiCuZn)N has relatively high ECSA, almost 2-fold than that of (Co)N. ECSA-normalized LSV curves show that (FeCoNiCuZn)N also exhibits the best OER activity [Supplementary Figure 6], indicating that both the enhanced intrinsic activity and the increased number of active sites enhance the OER performance.

Apart from the excellent activity, the electrochemical stability of (FeCoNiCuZn)N was evaluated by multi-potential and multi-current step tests (rapid response and short-term stability), as well as the

chronopotentiometry curve (long-term stability). It is found that the cycling stability of (FeCoNiCuZn)N was studied at various potentials [Figure 4E, left] and current densities [Figure 4E, right], in which the selected current densities and potentials were well retained, respectively. In addition, the potential change was almost negligible when the electrode was measured at a constant current density of 400 mA cm⁻² for 30 h [Figure 4F], verifying their preliminary yet substantial assessment of potential practical applications.

Mechanistic investigations

To investigate the mechanism behind the enhanced electrochemical performance, XPS, XANES, and extended EXAFS measurements were conducted. As illustrated in Supplementary Figure 7 and Figure 2B, unary (Co)N only shows Co²⁺, while Co²⁺ and Co³⁺ co-exist in the (FeCoNiCuZn)N samples. Furthermore, the Co 2p spectrum exhibits positive shifts with an increasing number of metal elements. Meanwhile, the Fe, Ni, Cu, and Zn peaks in (FeCoNiCuZn)N shift to the higher binding energy compared with those of the related UMNs [Supplementary Figures 8-11]. In other words, accompanied by metal addition, the metal ions in (FeCoNiCuZn)N exhibit higher oxidation states, indicating the change in the local coordination situation^[11].

The electronic structure and coordination environment of (FeCoNiCuZn)N were further confirmed through XANES and EXAFS experiments. In the Co K-edge XANES [Figure 5A], the Co K-edge position of (Co)N closely matches that of CoO, indicating a +2 oxidation state. However, for (FeCoNiCuZn)N, the Co K-edge lies between CoO and Co₃O₄. A slightly enhanced and right-shifted white line peak in (FeCoNiCuZn)N compared to (Co)N suggests an increased oxidation state of Co^[37,38]. Figure 5B presents a typical EXAFS fitting of (FeCoNiCuZn)N, which renders a bond distance of 2.10 Å and a CN of 7.55. The local coordination geometry of the two samples is further confirmed by their FT R-space spectra [Figure 5C], where both (Co)N and (FeCoNiCuZn)N display a prominent Co-N bond scattering feature that is inconspicuous as that of the Co foil. FT curve fitting [Supplementary Table 3] reveals that the Co-N coordination number decreases from 6.4 in (Co)N to 5.6 in (FeCoNiCuZn)N, while the bond length increases from 2.09 to 2.13 Å, indicating the existence of dangling bonds and structural distortion. It was also observed that the first shell peaks in the EXAFS spectrum of R space of all Fe, Co, Ni, Cu, and Zn elements exhibit only a slight mismatch [Figure 5D], indicating that the (FeCoNiCuZn)N is not completely in random and some short-range chemical ordering exists^[39,40]. This structural distortion is further supported by wavelet transform (WT) analysis [Figure 5E], which highlights differences in the local atomic arrangements of cobalt. Nitrogen functions as a structural and electronic modifier within the HEN framework, improving both chemical stability and electrical conductivity, which are crucial for enhancing catalytic efficiency in the OER^[18,27]. Obviously, the severe structural distortion is positive for the high oxidation state of Co, which is in favor of the further electrocatalysis process^[41-44].

The structure and composition of (FeCoNiCuZn)N after long-term stability were also evaluated by SEM, TEM, and XPS tests. As Supplementary Figure 12 shows, the spherical morphology of (FeCoNiCuZn)N is retained after the OER test. Additionally, the energy-dispersive X-ray spectroscopy (EDS) analysis further confirms the uniform distributions of all the metals [Supplementary Figure 13]. The survey and related high-resolution XPS spectrum of the (FeCoNiCuZn)N after OER were shown in Supplementary Figure 14. It is apparent that the Co³⁺ species increase after OER reaction [Supplementary Figure 14A], indicating that the oxidation of cobalt takes place and Co serves as an electron donor. In addition, the oxidation state of iron and nickel elements shows negligible variation in composition [Supplementary Figure 14B and C], implying Fe and Ni may play a role in structure stability. Furthermore, both Cu 2p and Zn 2p peaks of the (FeCoNiCuZn)N after OER shift to lower binding energy [Supplementary Figure 14D and E], which implies that Cu and Zn would act as electron acceptors to Co in the electrocatalysis process. Given the above analysis, we can clearly see that the synergy effect among the metals in (FeCoNiCuZn)N is conducive to

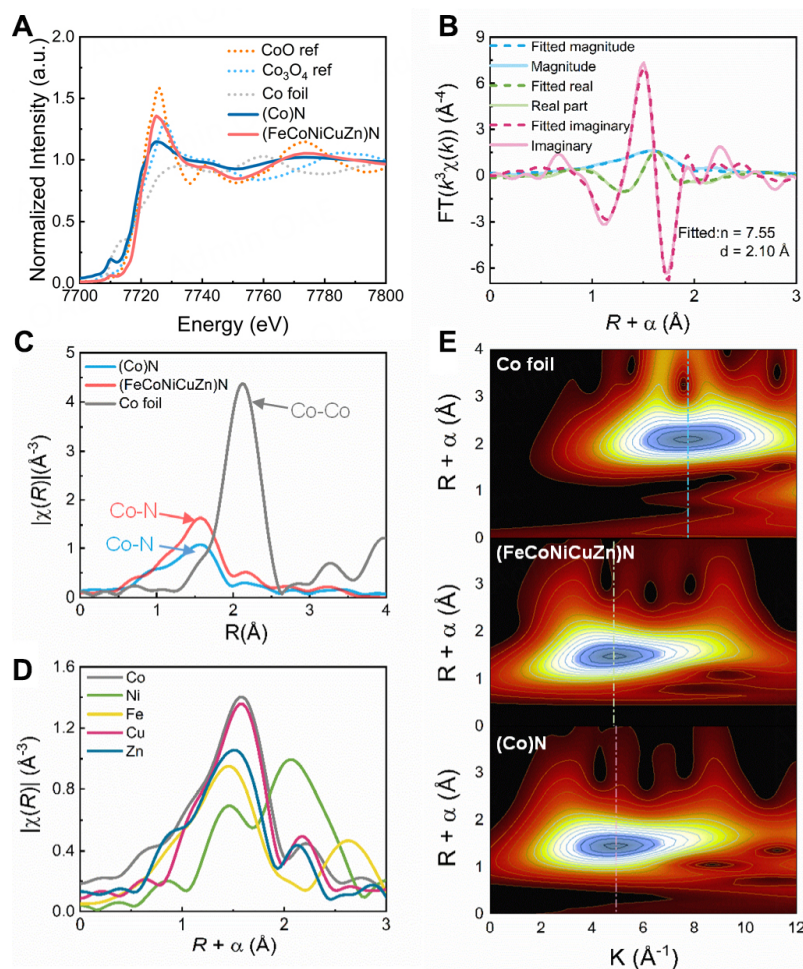


Figure 5. X-ray absorption spectroscopy of samples. (A) Co K-edge XANES spectra of Co foil, CoO, Co_3O_4 , (Co)N, and (FeCoNiCuZn)N; (B) EXAFS fitting of (FeCoNiCuZn)N; (C) Fourier transform (FT) of the Co K-edge EXAFS spectra of Co foil, (Co)N, and (FeCoNiCuZn)N; (D) The corresponding EXAFS fitting curve of Co-(FeCoNiCuZn)N: Fe (yellow), Co (grey), Ni (green), Cu (pink), and Zn (blue); (E) the WT contour plot of Co foil, (Co)N, and (FeCoNiCuZn)N.

boosting OER performance. Moreover, the metal-N content shows no significant variation [Supplementary Figure 14F], indicating the preservation of the original high-entropy metal nitride structure, suggesting that the catalytic performance is primarily affected by the engineered composition and nanostructure of the HEN. The following key aspects of high-entropy engineering contribute to the superior OER performance of (FeCoNiCuZn)N. First, (FeCoNiCuZn)N demonstrates enhanced structural stability due to lattice distortion caused by the incorporation of multiple elements. This structural reinforcement improves stability during electrochemical reactions. Second, synergistic effects arise from the diverse metal atoms in HENs, introducing a variety of catalytic sites and coordination environments, which enhance OER catalytic performance. Finally, high-entropy engineering modifies the electronic structure of the material, optimizing charge transfer, increasing the density of active sites, and lowering reaction overpotentials, all of which are crucial for efficient OER performance. Therefore, these results above demonstrate the synergistic effect of electron modulation and entropy stabilization on the (FeCoNiCuZn)N, which are closely correlated with the superior OER of (FeCoNiCuZn)N.

CONCLUSION

In conclusion, a noble metal-free HMN (FeCoNiCuZn)N was synthesized for the first time as an efficient OER electrocatalyst. Thermodynamic characterization indicates that both enthalpy and spontaneous entropy contributions favor a negative ΔG , enabling a low-temperature DES-aided solvothermal synthesis process. The synthesized (FeCoNiCuZn)N, composed of five evenly dispersed metals (Fe, Co, Ni, Cu, and Zn), exhibits efficient d-orbital electron transfer, enhancing its electronic structure. Additionally, the short-range ordering and complex composition generate a multidomain structure that promotes electron-lattice coupling, further boosting OER performance. As a result, the (FeCoNiCuZn)N demonstrates exceptional OER activity and enhanced durability. This work not only introduces a novel HMN material with excellent OER performance but also establishes a new pathway for fabricating HEMs with potential applications in energy conversion and storage catalysis.

DECLARATIONS

Author's contributions

Conceived the idea, wrote the manuscript, and provided financial support: Jiang, J.

Assisted in the collection of literature and scientific research drawings: Xu, Y.; Wang, Z.; Zhang, H.

Supervised and guided the academic expression of this work: Xu, Q.; Li, Y.

Availability of data and materials

The data that support the findings of this study are available from the corresponding author upon reasonable request.

Financial support and sponsorship

This work was supported by the National Natural Science Foundation of China (21903070), Advantageous Discipline Cultivation Joint Fund of Henan Province (No. 22610031), Basic Research Training of Zhengzhou University (No. 32213900) and the China Scholarship Council (202207045006).

Conflicts of interest

All authors declared that there are no conflicts of interest.

Ethical approval and consent to participate

Not applicable.

Consent for publication

Not applicable.

Copyright

© The Author(s) 2025.

REFERENCES

1. Hsu, W. L.; Tsai, C. W.; Yeh, A. C.; Yeh, J. W. Clarifying the four core effects of high-entropy materials. *Nat. Rev. Chem.* **2024**, *8*, 471-85. [DOI](#) [PubMed](#)
2. Yao, Y.; Dong, Q.; Brozena, A.; et al. High-entropy nanoparticles: synthesis-structure-property relationships and data-driven discovery. *Science* **2022**, *376*, eabn3103. [DOI](#)
3. Ma, Y.; Ma, Y.; Wang, Q.; et al. High-entropy energy materials: challenges and new opportunities. *Energy. Environ. Sci.* **2021**, *14*, 2883-905. [DOI](#)
4. Cantor, B.; Chang, I. T. H.; Knight, P.; Vincent, A. J. B. Microstructural development in equiatomic multicomponent alloys. *Mater. Sci. Eng. A.* **2004**, *375-7*, 213-8. [DOI](#)
5. Yeh, J. W.; Chen, S. K.; Lin, S. J.; et al. Nanostructured high-entropy alloys with multiple principal elements: novel alloy design concepts and outcomes. *Adv. Eng. Mater.* **2004**, *6*, 299-303. [DOI](#)

6. Zhang, Y.; Wang, D.; Wang, S. High-entropy alloys for electrocatalysis: design, characterization, and applications. *Small* **2022**, *18*, e2104339. DOI
7. Jiang, B.; Yu, Y.; Cui, J.; et al. High-entropy-stabilized chalcogenides with high thermoelectric performance. *Science* **2021**, *371*, 830-4. DOI
8. Ren, J. T.; Chen, L.; Wang, H. Y.; Yuan, Z. Y. High-entropy alloys in electrocatalysis: from fundamentals to applications. *Chem. Soc. Rev.* **2023**, *52*, 8319-73. DOI
9. Guo, R.; Yang, Y.; Zhao, C.; et al. The role of high-entropy materials in lithium-based rechargeable batteries. *Adv. Funct. Mater.* **2024**, *34*, 2313168. DOI
10. Liu, Z. Y.; Liu, Y.; Xu, Y.; et al. Novel high-entropy oxides for energy storage and conversion: from fundamentals to practical applications. *Green. Energy. Environ.* **2023**, *8*, 1341-57. DOI
11. Cui, M.; Yang, C.; Li, B.; et al. High-entropy metal sulfide nanoparticles promise high-performance oxygen evolution reaction. *Adv. Energy. Mater.* **2021**, *11*, 2002887. DOI
12. He, R.; Yang, L.; Zhang, Y.; et al. A CrMnFeCoNi high entropy alloy boosting oxygen evolution/reduction reactions and zinc-air battery performance. *Energy. Storage. Mater.* **2023**, *58*, 287-98. DOI
13. Li, K.; He, J.; Guan, X.; et al. Phosphorus-modified amorphous high-entropy CoFeNiCrMn compound as high-performance electrocatalyst for hydrazine-assisted water electrolysis. *Small* **2023**, *19*, e2302130. DOI
14. Zhang, Y.; Kang, J.; Xie, H.; et al. Boosting the oxygen evolution of high-entropy (oxy)hydroxide epitaxially grown on high entropy alloy by lattice oxygen activation. *Appl. Catal. B. Environ.* **2024**, *341*, 123331. DOI
15. Hooch, A. W.; Lee, S.; Lee, H. S.; et al. High-valence metal-driven electronic modulation for boosting oxygen evolution reaction in high-entropy spinel oxide. *Adv. Funct. Mater.* **2024**, *34*, 2309438. DOI
16. Nguyen, T. X.; Liao, Y. C.; Lin, C. C.; Su, Y. H.; Ting, J. M. Advanced high entropy perovskite oxide electrocatalyst for oxygen evolution reaction. *Adv. Funct. Mater.* **2021**, *31*, 2101632. DOI
17. Quan, L.; Jiang, H.; Mei, G.; Sun, Y.; You, B. Bifunctional electrocatalysts for overall and hybrid water splitting. *Chem. Rev.* **2024**, *124*, 3694-812. DOI
18. Luo, Q.; Lu, C.; Liu, L.; Zhu, M. A review on the synthesis of transition metal nitride nanostructures and their energy related applications. *Green. Energy. Environ.* **2023**, *8*, 406-37. DOI
19. Saidi, W. A. Emergence of local scaling relations in adsorption energies on high-entropy alloys. *NPJ. Comput. Mater.* **2022**, *8*, 86. DOI
20. Zhang, W.; Wei, X.; Wu, T.; et al. Carbothermal shock enabled functional nanomaterials for energy-related applications. *Nano. Energy.* **2023**, *118*, 108994. DOI
21. Ritter, T. G.; Pappu, S.; Shahbazian-Yassar, R. Scalable synthesis methods for high-entropy nanoparticles. *Adv. Energy. Sustain. Res.* **2024**, *5*, 2300297. DOI
22. Yao, Y.; Huang, Z.; Xie, P.; et al. Carbothermal shock synthesis of high-entropy-alloy nanoparticles. *Science* **2018**, *359*, 1489-94. DOI
23. Yu, D.; Xue, Z.; Mu, T. Correction: eutectics: formation, properties, and applications. *Chem. Soc. Rev.* **2021**, *50*, 9345. DOI
24. Deng, R.; Gao, M.; Zhang, B.; Zhang, Q. Solvent-mediated synthesis of functional powder materials from deep eutectic solvents for energy storage and conversion: a review. *Adv. Energy. Mater.* **2024**, *14*, 2303707. DOI
25. Yu, D.; Jiang, D.; Xue, Z.; Mu, T. Deep eutectic solvents as green solvents for materials preparation. *Green. Chem.* **2024**, *26*, 7478-507. DOI
26. Yang, H.; Cheng, Z.; Wu, P.; Wei, Y.; Jiang, J.; Xu, Q. Deep eutectic solvents regulation synthesis of multi-metal oxalate for electrocatalytic oxygen evolution reaction and supercapacitor applications. *Electrochim. Acta.* **2022**, *427*, 140879. DOI
27. Jiang, J.; Yan, P.; Zhou, Y.; et al. Interplanar growth of 2D non-van der waals Co₂N-based heterostructures for efficient overall water splitting. *Adv. Energy. Mater.* **2020**, *10*, 2002214. DOI
28. Barnes, A. J.; Le Gall, L.; Lauransan, J. Vibrational spectra of barbituric acid derivatives in low-temperature matrices: Part 2. Barbituric acid and 1,3-dimethyl barbituric acid. *J. Mol. Struct.* **1979**, *56*, 15-27. DOI
29. Alparone, A. Anharmonic IR and Raman spectra and electronic and vibrational (hyper)polarizabilities of barbituric, 2-thiobarbituric and 2-selenobarbituric acids. *Spectrochim. Acta. A. Mol. Biomol. Spectrosc.* **2014**, *117*, 669-78. DOI PubMed
30. Xu, Y.; Cheng, Z.; Jiang, J.; Du, J.; Xu, Q. 2D amorphous bi-metallic NiFe nitrides for a high-efficiency oxygen evolution reaction. *Chem. Commun.* **2021**, *57*, 13170-3. DOI
31. Wei, Y.; Xu, Y.; Zhang, H.; Jiang, J.; Xu, Q. Anion-regulated 2D amorphous binary nickel-iron nitrides for efficient water oxidation at high-current-densities. *New. J. Chem.* **2024**, *48*, 11206-10. DOI
32. Wu, Y.; Cai, J.; Xie, Y.; et al. Regulating the interfacial electronic coupling of Fe₂N via orbital steering for hydrogen evolution catalysis. *Adv. Mater.* **2020**, *32*, e1904346. DOI
33. Li, S.; Wang, S.; He, J.; et al. Chromium-doped nickel oxide and nickel nitride mediate selective electrocatalytic oxidation of steroid intermediates coupled with H₂ evolution. *Angew. Chem. Int. Ed.* **2023**, *62*, e202306553. DOI
34. Tiwari, A. P.; Bae, G.; Yoon, Y.; et al. Chemical strain engineering of copper atoms on continuous three-dimensional-nanopatterned nickel nitride to accelerate alkaline hydrogen evolution. *ACS. Sustain. Chem. Eng.* **2023**, *11*, 5229-37. DOI
35. Mann, D. S.; Kwon, S. N.; Thakur, S.; Patil, P.; Jeong, K. U.; Na, S. I. Suppressing redox reactions at the perovskite-nickel oxide interface with zinc nitride to improve the performance of perovskite solar cells. *Small* **2024**, *20*, e2311362. DOI PubMed

36. Chen, J.; Wang, D.; Yang, X.; et al. Accelerated transfer and spillover of carbon monoxide through tandem catalysis for kinetics-boosted ethylene electrosynthesis. *Angew. Chem. Int. Ed.* **2023**, *62*, e202215406. DOI
37. Li, J.; Meng, X.; Song, X.; et al. Valence engineering via manganese-doping on cobalt nitride nanoarrays for efficient electrochemically paired glycerol valorization and H₂ production. *Adv. Funct. Mater.* **2024**, *34*, 2316718. DOI
38. Yan, Q.; Feng, J.; Shi, W.; et al. Chromium-induced high covalent Co-O bonds for efficient anodic catalysts in PEM electrolyzer. *Adv. Sci.* **2024**, *11*, e2402356. DOI PubMed PMC
39. Yao, Y.; Liu, Z.; Xie, P.; et al. Computationally aided, entropy-driven synthesis of highly efficient and durable multi-elemental alloy catalysts. *Sci. Adv.* **2020**, *6*, eaaz0510. DOI PubMed PMC
40. Li, Y.; Zhang, B.; Wang, W.; et al. Selective-etching of MOF toward hierarchical porous Mo-doped CoP/N-doped carbon nanosheet arrays for efficient hydrogen evolution at all pH values. *Chem. Eng. J.* **2021**, *405*, 126981. DOI
41. Xiong, D.; He, X.; Liu, X.; et al. 1D/3D heterogeneous assembling body of cobalt nitrides for highly efficient overall hydrazine splitting and supercapacitors. *Small* **2024**, *20*, e2306100. DOI
42. Li, Y.; Mao, Z.; Wang, Q.; et al. Hollow nanosheet array of phosphorus-anion-decorated cobalt disulfide as an efficient electrocatalyst for overall water splitting. *Chem. Eng. J.* **2020**, *390*, 124556. DOI
43. Tian, Y.; Li, S.; Huang, R.; et al. Rational construction of core-branch Co₃O₄@CoNi-layered double hydroxide nanoarrays as efficient electrocatalysts for oxygen evolution reaction. *J. Alloys. Compd.* **2022**, *899*, 163259. DOI
44. Zhang, L.; Cai, W.; Bao, N. Top-level design strategy to construct an advanced high-entropy Co-Cu-Fe-Mo (Oxy)hydroxide electrocatalyst for the oxygen evolution reaction. *Adv. Mater.* **2021**, *33*, e2100745. DOI